Numerical simulation of the aerobreakup of a water droplet

Jomela C. Meng[1],† **and Tim Colonius**[1]

[1]California Institute of Technology, Pasadena, CA 91125, USA

We present a three-dimensional numerical simulation of the aerobreakup of a spherical water droplet in the flow behind a normal shock wave. The droplet and surrounding gas flow are simulated using the compressible multicomponent Euler equations in a finite-volume scheme with shock and interface capturing. The aerobreakup process is compared with available experimental visualizations. Features of the droplet deformation and breakup in the stripping breakup regime, as well as descriptions of the surrounding gas flow, are discussed. Analyses of observed surface instabilities and a Fourier decomposition of the flow field reveal asymmetrical azimuthal modulations and broadband instability growth that result in chaotic flow within the wake region.

Key words: breakup/coalescence, drops, shock waves

---

1. Introduction

The study of droplet aerobreakup has historically been motivated by three applications: bulk dissemination of liquid agents, raindrop damage during supersonic flight, and secondary atomization of liquid jets in turbomachinery. Much of the aerobreakup literature has focused research efforts on characterizing and mapping various breakup regimes (e.g. Lane 1951; Engel 1958; Hanson, Domich & Adams 1963; Ranger & Nicholls 1968; Hsiang & Faeth 1995), calculating characteristic breakup times (e.g. Ranger & Nicholls 1968; Hsiang & Faeth 1992), quantifying dependence on parameters such as density and viscosity ratios (e.g. Hanson *et al.* 1963; Theofanous *et al.* 2012), predicting final drop size distributions (e.g. Ranger & Nicholls 1968; Pilch & Erdman 1987), and quantifying unsteady drag properties (e.g. Engel 1958; Simpkins & Bales 1972; Joseph, Belanger & Beavers 1999). Unfortunately, these experimental and theoretical research efforts have resulted in many, and often conflicting, phenomenological models describing the aerobreakup process, and to date, a definitive understanding of aerobreakup remains elusive (Khosla, Smith & Throckmorton 2006).

Beginning with the work of Hinze (1949), the Weber number, $We = \rho_g u_g^2 D_0 / \sigma$, has been the principal parameter used to delineate the various regimes of aerobreakup. Traditionally, there exist five distinct regimes that are well established in the literature (Pilch & Erdman 1987; Guildenbecher, López-Rivera & Sojka 2009). They are,

---

in order of increasing *We*, the vibrational, bag, bag-and-stamen, stripping, and catastrophic regimes.

The stripping regime, which is of primary interest in this paper, marks a transition in breakup physics that fundamentally differs from that of the preceding breakup regimes. Generally speaking, the stripping regime is characterized by an initial deformation of the droplet into a disk-like shape. Following the shape change, droplet fluid is observed to be stripped from the droplet's periphery in a region near the droplet equator (defined as a polar, or inclination, angle of $\varphi = \pi/2$). Ranger & Nicholls ([1968](#)) postulated the 'boundary layer stripping' or 'shear stripping' model, where boundary layers both inside and outside the drop become unstable at the droplet equator, and are subsequently stripped off by the ambient gas flow. Liu & Reitz ([1997](#)) later proposed an alternate mechanism known as 'sheet thinning', where the droplet is initially flattened by the pressure gradient between the drop's poles ($\varphi = 0, \pi$) and equator. Once flattened, the strong inertial forces from the surrounding flow draw a thin sheet of liquid off the periphery. This sheet is accelerated, stretched, and bent in the direction of flow, and eventually breaks up into streamwise ligaments that fragment into individual drops. Due to the flattened disk-like shape of the deformed droplet, flow separation occurs for all practical values of the Reynolds number, $Re = \rho_g u_g D_0 / \mu_g$, and the sheet thinning mechanism can be considered an inviscid phenomenon with no dependence on *Re* (Guildenbecher *et al.* [2009](#)).

The instability of the thin liquid sheet that is drawn from the droplet's periphery in the sheet thinning model is thought to be responsible for the generation of product droplets. Liu & Reitz ([1997](#)) described a 'stretched streamwise ligament breakup' mechanism wherein, for low liquid flow rates of a planar liquid sheet sandwiched between two shear air layers, streamwise vortical waves, alternating with thin liquid membranes, would grow along the sheet. The membranes would burst first due to the rotation of the streamwise vortices, leaving streamwise ligaments that subsequently broke up. More recently, Jalaal & Mehravaran ([2014](#)) attributed the breakup to the rise of Rayleigh–Taylor (RT) instability waves on the sheet. In this mechanism, the Kelvin–Helmholtz (KH) instability generates axisymmetric waves at the liquid–gas interface. The transient acceleration of these wave crests or rims (in the case of the liquid jet) into the downstream air triggers a RT instability, which produces 'transverse azimuthal modulations.'

Recent work by Theofanous, Li & Dinh ([2004](#)) studying aerobreakup in rarefied supersonic flows, and subsequent publications (Theofanous & Li [2008](#); Theofanous [2011](#); Theofanous *et al.* [2012](#)), has substantially changed the overall understanding of aerobreakup. Theofanous *et al.* ([2004](#)) proposed a reclassification into two principal breakup regimes: Rayleigh–Taylor piercing (RTP) and shear-induced entrainment (SIE). Theofanous & Li ([2008](#)) described SIE as a combination of shear-driven radial motion, which results in the flattening, as well as instabilities on the stretched liquid sheet. Perhaps most importantly, this reclassification argues that the catastrophic breakup regime does not exist. Theofanous & Li ([2008](#)) contended that the wavy interface on the upstream side of the droplet was an artefact created by a projected view of a complex flow field, and that no RT waves exist or pierce the drop. Using laser-induced fluorescence as their experimental visualization technique, SIE was proposed as the terminal regime for $We > 10^3$.

Recently, numerical simulation has emerged as a tool for studying aerobreakup. Unfortunately, due to the high computational costs of fully three-dimensional (3D) simulations, numerical aerobreakup studies have often invoked two-dimensional (2D) (Zaleski, Li & Succi [1995](#); Igra & Takayama [2001a](#),[b](#),[c](#); Chen [2008](#)) or

axisymmetric (Han & Tryggvason 2001; Aalburg, Leer & Faeth 2003; Wadhwa, Magi & Abraham 2007; Chang, Deng & Theofanous 2013) approximations. Additionally, fluid density ratios are often assumed to be small, or the fluids are considered to be incompressible (Han & Tryggvason 2001; Aalburg *et al.* 2003; Quan & Schmidt 2006; Jalaal & Mehravaran 2014; Xiao, Dianat & McGuirk 2014; Castrillon Escobar *et al.* 2015; Jain *et al.* 2015). Previous work from the authors (Meng & Colonius 2015) simulated the early stages of two-dimensional aerobreakup, with comparison to the experimental work of Igra & Takayama (2001*c*). Qualitative features of the breakup process, such as the presence of a transitory equatorial recirculation region and an upstream jet in the wake, were discussed. Additionally, a parametric study varying incident shock strength was performed to study the effects of the transition between subsonic and supersonic post-shock flow. A novel method of calculating the cylinder's centre-of-mass properties was also utilized to obtain accurate unsteady acceleration and drag histories.

   Using numerical simulation, the purpose of this paper is to elucidate the physical breakup mechanisms responsible for the fully three-dimensional, compressible aerobreakup of a single water droplet in air. While a direct numerical simulation would be ideal for such an investigation, the computational grid required to fully resolve all scales of the aerobreakup problem is intractable on currently available computational resources; a compromise must be made. We thus consider the 'inviscid' case, which is in turn regularized by artificial viscosity and numerical diffusion of the interface. The effects of these approximations are discussed in detail in § 3.2. Additionally, we will attempt to interpret the numerical results in a manner consistent with the uncertainties introduced by the approximations. These results fill a gap in the current state of droplet aerobreakup knowledge associated with the underlying fundamental flow physics that dictates the experimentally observed phenomena. Building upon the computational efforts of Coralic & Colonius (2014), we utilize a compressible multicomponent flow solver to numerically investigate this fundamental fluid dynamics problem. The rest of this paper is organized as follows. In § 2, we describe the problem set-up and introduce the governing equations. The numerical algorithm is subsequently described in § 3, along with the calculation of various flow quantities used in the analysis. We describe the evolution of the liquid droplet, show its centre-of-mass properties, and compare with available experimental visualizations in §§ 4, 4.1 and 4.2. The flow field in the gas phase is investigated in § 4.3. The mechanisms of surface instabilities are discussed in § 5.1, and are followed by a Fourier decomposition analysis in § 5.2. Finally, concluding remarks are made in § 6.

2. Physical modelling

2.1. *Problem description*

In the laboratory, shock tubes are most often used to generate large relative velocities between the liquid droplet and surrounding gas flow. Normal shock waves, in and of themselves, have little effect on the droplet. Instead, they serve as a reliable and repeatable way to create a high-speed flow around the droplet, which is responsible for the droplet's subsequent deformation and disintegration (Hanson *et al.* 1963; Ranger & Nicholls 1968; Joseph *et al.* 1999). In figure 1, a schematic is shown of the initial condition and computational grid. The shock wave of strength $M_s = 1.47$ (modelled as a step discontinuity in fluid properties) is travelling in air towards the water droplet, which is initialized as a spherical interface with diameter D_0 on the cylindrical grid. The drop and the ambient air downstream of the shock are
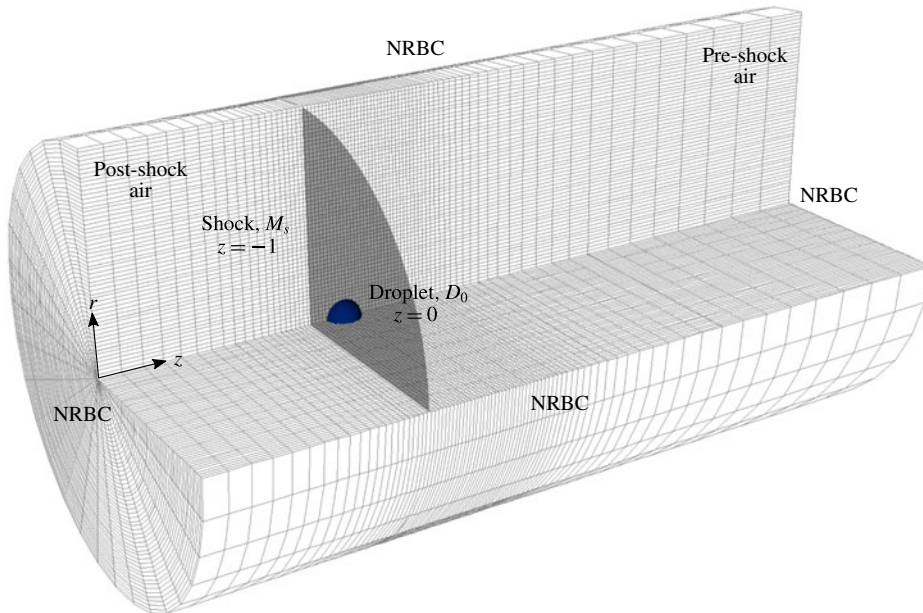
FIGURE 1. (Colour online) Schematic of the 3D initial condition and non-uniform computational domain at 1:10 of the actual resolution. The grid extends radially outward for $6D_0$, and the axial extents are $-7D_0 \leqslant z \leqslant 15.5D_0$.

initialized at rest. The entire 3D flow field is simulated with no enforced symmetries. Non-reflective boundary conditions (NRBC), applied at all computational domain boundaries, approximately extend the surrounding air to infinity. The simulation is performed on the computational domain $\Omega = [-7D_0, 15.5D_0] \times [0, 6D_0] \times [0, 2\pi]$ with a spatial resolution of $(N_z, N_r, N_\theta) = (800, 600, 320)$ grid cells. The grid is stretched towards the axial boundaries using a hyperbolic tangent function. The most refined portion of the grid is located near the initial location of the droplet and in the region of the near-field wake. In this region, the nominal axial and radial grid resolution corresponds to 100 cells per original droplet diameter. The azimuthal resolution is chosen such that the cells near the spherical droplet interface are close to regular. Previous testing of grid resolution sensitivities in 2D (Meng & Colonius 2015; Meng 2016) suggests the present spatial resolution captures the salient flow features without being computationally cumbersome. The simulation is performed with a constant Courant–Friedrichs–Lewy (CFL) number of 0.2. Since the initial condition is axisymmetric, the gas is initially seeded with small random radial and azimuthal velocity perturbations, the largest of which have approximate magnitudes of $O(10^{-4}u_s)$, where u_s is the post-shock gas velocity. These white-noise-type perturbations are generated via the Fortran compiler's intrinsic random number generator, and are applied to both the pre-shock and post-shock gas in the initial condition.

2.2. *Governing equations*

We model the flow with the compressible multicomponent Euler equations. In addition to being compressible, each fluid is considered immiscible and does not undergo phase change. In the absence of mass transfer and surface tension, material interfaces are

simply advected by the local flow velocity. For a system of two fluids, this gives rise to a five-equation model, introduced in its inviscid form by Allaire, Clerc & Kokh (2002). Implications of the choice to neglect viscous and capillary effects are addressed in detail in §3.2. The five-equation model, (2.1), consists of individual continuity equations for each of the fluids, (2.1a) and (2.1b), mixture momentum, (2.1c), and energy, (2.1d), equations, and a transport equation for the gas volume fraction, (2.1e):

$$\frac{\partial(\alpha_g \rho_g)}{\partial t} + \boldsymbol{\nabla} \cdot (\alpha_g \rho_g \boldsymbol{u}) = 0, \tag{2.1a}$$

$$\frac{\partial(\alpha_l \rho_l)}{\partial t} + \boldsymbol{\nabla} \cdot (\alpha_l \rho_l \boldsymbol{u}) = 0, \tag{2.1b}$$

$$\frac{\partial(\rho \boldsymbol{u})}{\partial t} + \boldsymbol{\nabla} \cdot (\rho \boldsymbol{u} \otimes \boldsymbol{u} + p\boldsymbol{I}) = \boldsymbol{0}, \tag{2.1c}$$

$$\frac{\partial E}{\partial t} + \boldsymbol{\nabla} \cdot ((E + p)\boldsymbol{u}) = 0, \tag{2.1d}$$

$$\frac{\partial \alpha_g}{\partial t} + \boldsymbol{u} \cdot \boldsymbol{\nabla} \alpha_g = 0, \tag{2.1e}$$

where ρ is the density, α is the volume fraction, $\boldsymbol{u}$ is the velocity vector, p is the pressure, E is the total energy defined as $E = \rho\varepsilon + (1/2)\rho\|\boldsymbol{u}\|^2$, ε is the specific internal energy, and the subscripted g, l represent, respectively, the gas and liquid fluids. Each equation in the five-equation model, (2.1), is evolved independently of all others. While alternate models for multicomponent flows exist within the literature (e.g. Kapila *et al.* 2001; Murrone & Guillard 2005; Saurel, Petitpas & Berry 2009; Pelanti & Shyue 2014), the present model is chosen for its simplicity and desirable conservation properties. The simplified interface model theoretically ensures volume fraction positivity, and does not require regularization to fully specify shock jump conditions. Though it is not capable of physically handling mixture regions, the model is sufficient for the immiscible fluids assumed in the multicomponent flows of interest.

The simulation of material interfaces is made possible by the volume-of-fluid method, which belongs to the broader class of interface-capturing schemes. One common characteristic of these schemes is the relaxation of the natural sharpness of material discontinuities. That is, the interfaces are allowed to numerically diffuse, resulting in an interface region of small, but finite, thickness. Within this interface region, a non-physical fluid mixture exists, which is appropriately treated using mixture rules that are defined in §2.2.1. For numerical stability purposes, material interfaces are not initialized as sharp discontinuities, but are smeared over a few grid cells. Based on previous results (Johnsen 2007; Coralic 2015) and sensitivity testing by the authors for the specific problem of aerobreakup, this initial artificial smearing over a few cells is known to have negligible impact on the computational results.

2.2.1. *Equation of state*

The five-equation model, (2.1), is closed with the specification of an appropriate equation of state (EOS) that relates the fluid densities, pressures, and internal energies. The stiffened gas EOS (Harlow & Amsden 1971), is used in our flow solver to model both gases and liquids:

$$p = (\gamma - 1)\rho\varepsilon - \gamma\pi_\infty, \tag{2.2}$$

Fluid	ρ (kg m^{-3})	c (m s^{-1})	γ	π_∞ (Pa)
Air	1.204	343	1.40	0
Water	1000	1450	6.12	3.43×10^8

TABLE 1. Fluid properties at normal temperature and pressure.

where γ and π_∞ are fitting parameters that are empirically derived from fluid shock Hugoniot data. The consistent EOS sound speed is calculated as

$$c = \sqrt{\frac{\gamma(p + \pi_\infty)}{\rho}}. \tag{2.3}$$

Given that the modelled fluids are considered to be immiscible, each fluid in the solver individually obeys the stiffened gas EOS. The properties for the fluids of interest, air and water, are tabulated in table 1. For air, $\pi_\infty = 0$ Pa, and the stiffened gas EOS reduces to the ideal gas law with γ as the specific heat ratio. The fitting parameters for water are based on the shock Hugoniot data of Gojani *et al.* (2016), following the fitting procedure described in Johnsen (2007).

Within the diffuse interface region, mixture rules must be defined for the properties of fluid mixtures. These mixture regions are an artefact of numerical diffusion, and are not representative of mixing on a molecular level. For a system of two fluids, expressions of the mixture volume fraction, density, and internal energy are commonly defined as

$$1 = \alpha_g + \alpha_l, \tag{2.4}$$

$$\rho = \alpha_g \rho_g + \alpha_l \rho_l, \tag{2.5}$$

$$\rho \varepsilon = \alpha_g \rho_g \varepsilon_g + \alpha_l \rho_l \varepsilon_l. \tag{2.6}$$

We note that (2.4) and (2.5) do not affect the independence of (2.1*a*) and (2.1*b*). Equations (2.1*a*), (2.1*b*) and (2.4) allow for the independent calculations of ρ_l and ρ_g, while (2.5) is used with (2.1*c*) to compute the velocity, $\boldsymbol{u}$. Following previous work, we define the following mixture rules for two functions of the stiffened gas EOS fitting parameters (Allaire *et al.* 2002):

$$\Gamma = \alpha_g \Gamma_g + \alpha_l \Gamma_l, \quad \Gamma = \frac{1}{\gamma - 1}, \tag{2.7a,b}$$

$$\Pi_\infty = \alpha_g \Pi_{\infty,g} + \alpha_l \Pi_{\infty,l}, \quad \Pi_\infty = \frac{\gamma \pi_\infty}{\gamma - 1}. \tag{2.8a,b}$$

2.2.2. *Non-dimensionalization conventions*

In our simulation, the five-equation model, (2.1), is solved in dimensionless form. Unless otherwise specified, non-dimensionalization of the variables is done using the initial droplet diameter D_0, and post-shock gas velocity u_s, pressure p, and density ρ_s. The resulting change in variables is

$$t^* = t\frac{u_s}{D_0}\sqrt{\frac{\rho_s}{\rho_l}}, \quad x^* = \frac{\boldsymbol{x}}{D_0}, \quad \rho^* = \frac{\rho}{\rho_s}, \quad \boldsymbol{u}^* = \frac{\boldsymbol{u}}{u_s}, \quad p^* = \frac{p}{p_s}, \tag{2.9a-e}$$

where the superscripted asterisk denotes a non-dimensional quantity. The additional density ratio in the definition of t^* results in a non-dimensional breakup time ubiquitously found within the aerobreakup literature (e.g. Ranger & Nicholls 1968; Simpkins & Bales 1972; Guildenbecher *et al.* 2009). This characteristic transport time is 'derived from analysis of the drop displacement assuming constant acceleration due to drag...' (Guildenbecher *et al.* 2009) and is 'characteristic of drop breakup by Rayleigh–Taylor or Kelvin–Helmholtz instabilities...' (Pilch & Erdman 1987).

3. Numerical method

The Multicomponent Flow Code (MFC) is a research flow solver capable of solving the compressible Navier–Stokes equations for multicomponent flows. The numerical method, which is both shock and interface capturing, is based on the work on Johnsen & Colonius (2006). Since its development, MFC has been used to study non-spherical bubble collapse (Johnsen 2007; Johnsen & Colonius 2009) and shock-induced collapse of bubbles inside deformable vessels (Coralic & Colonius 2013). Verification of the algorithm via benchmark test cases and parallel performance metrics have previously been documented (Coralic & Colonius 2014; Coralic 2015; Meng 2016), and are not reproduced here. Instead, we present only a high-level overview of the numerical algorithm, and direct interested readers to the referenced publications for additional details.

3.1. *Spatial and temporal discretizations*

The five-equation model, (2.1), is spatially discretized on a 3D cylindrical grid in the following form:

$$\frac{\partial \boldsymbol{q}}{\partial t} + \frac{\partial \boldsymbol{f}(\boldsymbol{q})}{\partial z} + \frac{\partial \boldsymbol{g}(\boldsymbol{q})}{\partial r} + \frac{\partial \boldsymbol{h}(\boldsymbol{q})}{\partial \theta} = \boldsymbol{s}(\boldsymbol{q}), \tag{3.1}$$

where $\boldsymbol{q}$ is the vector of conservative variables, $\boldsymbol{f}(\boldsymbol{q}), \boldsymbol{g}(\boldsymbol{q})$, and $\boldsymbol{h}(\boldsymbol{q})$ are flux vectors in each of the coordinate directions, and $\boldsymbol{s}(\boldsymbol{q})$ is a source term vector (see details in appendix A). In cylindrical coordinates, the divergence operator on an arbitrary vector $\boldsymbol{v} = (v_z, v_r, v_\theta)^{\mathrm{T}}$ is

$$\nabla \cdot \boldsymbol{v} = \frac{\partial v_z}{\partial z} + \frac{\partial v_r}{\partial r} + \frac{v_r}{r} + \frac{1}{r}\frac{\partial v_\theta}{\partial \theta}. \tag{3.2}$$

Following Johnsen (2007), all v_r/r terms are treated as geometrical source terms in $\boldsymbol{s}(\boldsymbol{q})$. By discretizing the governing equations in this manner, the source terms account for all cylindrical geometry effects. The axis singularity is treated following Mohseni & Colonius (2000) with the definition of a new radial coordinate that spans both positive and negative radius, i.e.

$$\tilde{r}(r, \theta) = \begin{cases} r & \text{if } 0 \leqslant \theta < \pi, \\ -r & \text{if } \pi \leqslant \theta < 2\pi. \end{cases} \tag{3.3}$$

Additional details of the numerical method, as well as its verification and validation, can be found in Meng (2016). Within the finite-volume formulation, the reconstruction of the state variables at the cell boundaries is performed using a third-order weighted essentially non-oscillatory (WENO) scheme developed for Cartesian coordinates. Using the Cartesian WENO weights and polynomials, formal order of accuracy is retained in the axial and radial coordinates, while not guaranteed in the azimuthal coordinate. Convergence studies of the numerical method, however, show that second-order accuracy is retained (Meng 2016). Finally, the system of equations is temporally integrated using a third-order total variation diminishing Runge–Kutta scheme.

3.2. *Modelling approximations and implications*

The governing equations of §2.2 are notably missing physical models for molecular viscosity and surface tension. While the algorithms required to implement viscous and capillary models in the governing equations are known (Meng 2016) (the five-equation model of Allaire *et al.* (2002) was subsequently extended to include viscous effects by Perigaud & Saurel (2005), and capillary effects can be modelled by including additional source terms), the computational resources required for such a direct numerical simulation are well beyond what is currently feasible. The present spatial resolution of $(N_z, N_r, N_\theta) = (800, 600, 320)$ is already a grid with 1.536×10^8 cells. For the high Reynolds numbers associated with aerobreakup in the SIE regime, the grid resolution requirements to reach grid convergence would be extraordinary. As an example, the axisymmetric work of Chang *et al.* (2013) employed an eight-level adaptive mesh refinement (AMR) scheme with an equivalent resolution of 800 points per diameter. In order to sufficiently resolve the viscous boundary layer, the AMR mesh had to be augmented with an additional body-fitted structured conformal mesh that had a spatial resolution of 4000 points per diameter. Taking even the coarsest resolution requirement of 800 cells per diameter would be an increase by a factor of 8 from the present resolution. Additionally, while it is more difficult to estimate a precise grid requirement for capillary effects, a conservative estimate of a factor of 10 in each coordinate direction would result in a requirement of $O(10^{14})$ grid points to reach *ab initio* physical fidelity. Even with AMR savings, we suspect this problem to be intractable. Therefore, while the physics can be (and has been) implemented with relative ease, the numerical viscosity would dominate these physical effects unless the above spatial resolutions were somehow achieved.

Given that a compromise must be made, we consider the 'inviscid' case without surface tension. Firstly, it is generally understood that so-called 'inviscid' simulations using shock- and interface-capturing schemes, i.e. those performed without explicit molecular viscosity modelling, inherently include numerical viscosity whose magnitude is dependent on the spatial resolution. This compromise thus precludes providing evidence of convergence, because such convergence will not exist when the flow becomes unstable and turbulent – the smallest length scales will be at the scale of the grid. It is clear that at the present spatial resolution, we are unable to capture fine-scale instabilities that might arise on the droplet's surface such as the KH waves experimentally observed by Theofanous *et al.* (2012) (recall that Chang *et al.* (2013) used a resolution of 4000 nodes per diameter to capture the viscous boundary layer). It should be noted that an inability to capture these fine-scale instabilities is solely a consequence of the employed spatial resolution. Interfacial instabilities (at least KH, RT, Richtmyer–Meshkov, and capillary) are driven by shear, which arises even in 'inviscid' simulations. For a solid surface, the no-slip condition, which of course requires the existence of viscosity, gives rise to shear, which in turn can drive both viscous (e.g. Tollmien–Schlichting) and inviscid instabilities. In the interface between two immiscible fluids, the conservation of momentum requires equality of the tangential viscous stresses, which in turn leads to a continuity of the velocity. In the true inviscid limit, the fluids would slip, but in the presence of any viscosity, and, indeed, any artificial viscosity, the velocity is again continuous. This leads to shear and, in turn, interfacial instabilities. With the exception of capillary instabilities, the five-equation model can support all the other mentioned surface instabilities, though they are not always adequately resolved.

The effects of surface tension in the aerobreakup problem become increasingly important with time. In particular, capillary instabilities are of primary importance

when it comes to the disintegration of the thin sheets of liquid that are stripped from the droplet's periphery (discussed in § 4). In the absence of surface tension modelling, there does not exist a numerical mechanism that approximates capillary effects, i.e. there is no capillary counterpart to numerical viscosity. Without such a mechanism, we do not capture the ultimate capillary-driven breakup mechanism of a droplet undergoing aerobreakup. Instead, the actual mechanism of breakup in the results is modelled in terms of numerical diffusion effects, i.e. breakup occurs as a consequence of numerical diffusion and finite spatial resolution. Given this modelling approximation, we expect the numerical results to have increasingly large uncertainties as time progresses. Nevertheless, the agreement we find with experimental results suggests that the important mechanisms are captured; a definitive quantification of the error awaits future work.

While traditional grid convergence cannot be shown for the present numerical results, we can estimate an approximate, effective Reynolds number associated with the numerical viscosity for the given grid. A series of tests using 2D viscous simulations (Meng & Colonius 2015; Meng 2016) indicate that the effective Reynolds number is no less than 500 at the spatial resolution of our 3D simulation. While this estimate is crude, and much lower than the corresponding experiments, it provides some assurance that we are in the inertia-dominated regime, where we might expect viscosity to play a small role at the scales of interest, at least at early times before the flow is fully turbulent and the droplet is disintegrated.

3.3. *Droplet diagnostics*

As the droplet undergoes aerobreakup, its centre-of-mass properties are of interest. Taking advantage of the type of quantitative analysis allowed by simulations, integral expressions have been derived (Meng & Colonius 2015) for the droplet's centre-of-mass velocity and acceleration that minimize unnecessary noise that would be introduced by differentiating position data:

$$x_c = \frac{\int_{\Omega} \alpha_l \rho_l x \, dV}{\int_{\Omega} \alpha_l \rho_l \, dV}, \quad (3.4)$$

$$u_c = \frac{dx_c}{dt} = \frac{\int_{\Omega} \alpha_l \rho_l u \, dV}{\int_{\Omega} \alpha_l \rho_l \, dV}, \quad (3.5)$$

$$a_c = \frac{d^2 x_c}{dt^2} = \frac{\int_{\Omega} \alpha_l \rho_l a \, dV}{\int_{\Omega} \alpha_l \rho_l \, dV}, \quad (3.6)$$

where the integrated volume is that of the entire computational domain, Ω. The liquid partial density, $\alpha_l \rho_l$, is then the parameter that restricts the integration to cells with non-zero liquid volume fractions. Additional details of the derivations of (3.4)–(3.6) can be found in Meng (2016). It should be noted that (3.5) and (3.6) are valid as long as the liquid mass in the domain, $m_l = \int_{\Omega} \alpha_l \rho_l \, dV$, remains a constant; once liquid mass flux through the domain boundaries is non-zero, we terminate their calculation.

Given that our volume-of-fluid numerical method involves a diffuse interface that is smeared across a few grid cells, isopleths and isosurfaces, representing the coherent droplet body in the following numerical results, are shown for multiple values of the liquid volume fraction, α_l. The impact of various choices of α_l on the interpretation of the numerical results is explicitly discussed in the respective results sections. Fortunately, the ambiguity in the exact interface location does not adversely impact the conclusions that are drawn from our results.

4. Droplet morphology

The evolution of the deforming droplet as observed from our simulation is first described with an emphasis on the behaviour of the liquid phase. Figure 2 shows an isometric view of isosurfaces of the liquid volume fraction. A quarter of the surface has been removed to reveal the interior isosurfaces. From figure 2, we observe that the morphology of the drop follows a distinct progression as the droplet is flattened. Initially, the deformed sphere takes on a muffin-like shape, with the top of the muffin oriented upstream. That is, the upstream side of the droplet remains nearly spherical, but is pushed into the liquid behind it, creating the muffin lip. The downstream side of the droplet is quickly compressed into a flat plane and remains so for a significant portion of the breakup. Two liquid sheets are observed during this deformation. The first is the established liquid sheet drawn from the droplet equator, while the second expands from the planar downstream side of the droplet. As the muffin-shaped droplet is compressed *en masse*, the liquid sheets eventually merge into a single sheet emanating from the droplet periphery. From figure 3, we see that the present spatial resolution is sufficient to resolve this liquid sheet, even at late times in the simulation. Since surface tension is not modelled, the disjoint interface is an artefact of numerical diffusion and finite resolution. From the sequence of images in figure 2, the liquid sheet is observed to radially flap, and the dynamic liquid structure is reminiscent of a swimming jellyfish. Furthermore, this liquid sheet forms an envelope for a large cavity that exists directly behind the flattened drop. Theofanous *et al.* (2012) experimentally observed this phenomenon (see figure 7) and described it as 'a cylindrical "curtain" around an empty space behind the coherent portion of the drop.' In the experiments, the curtain is composed of liquid fragments from the disintegrating liquid sheet. Our simulation, in the absence of surface tension, is unable to capture such a disintegration, though the small α_l-isovalue needed to visualize the sheet is indicative of its primarily gaseous composition. At approximately $t^* = 0.681$, the axisymmetry of the liquid sheet is lost as instabilities arise on the surface in the form of transverse azimuthal modulations, which are further discussed in § 5. At late times in the breakup process, the larger α_l-isosurfaces show the coherent droplet body as a large thin disk-like shape.

4.1. *Centre-of-mass properties*

The droplet's centre-of-mass drift, velocity, and acceleration in the streamwise (axial) direction are plotted in figure 4. While the drift curve appears to be roughly parabolic, the subsequent velocity and acceleration curves reveal that a constant acceleration assumption would be erroneous. Focusing on the acceleration curve, the initial spike in acceleration is the passage of the shock wave over the droplet. The maximum acceleration occurs when the shock reflection on the droplet's surface transitions from a regular reflection to a Mach reflection. This is further discussed in § 4.3. Following this initial spike, we note the existence of a brief period immediately following the
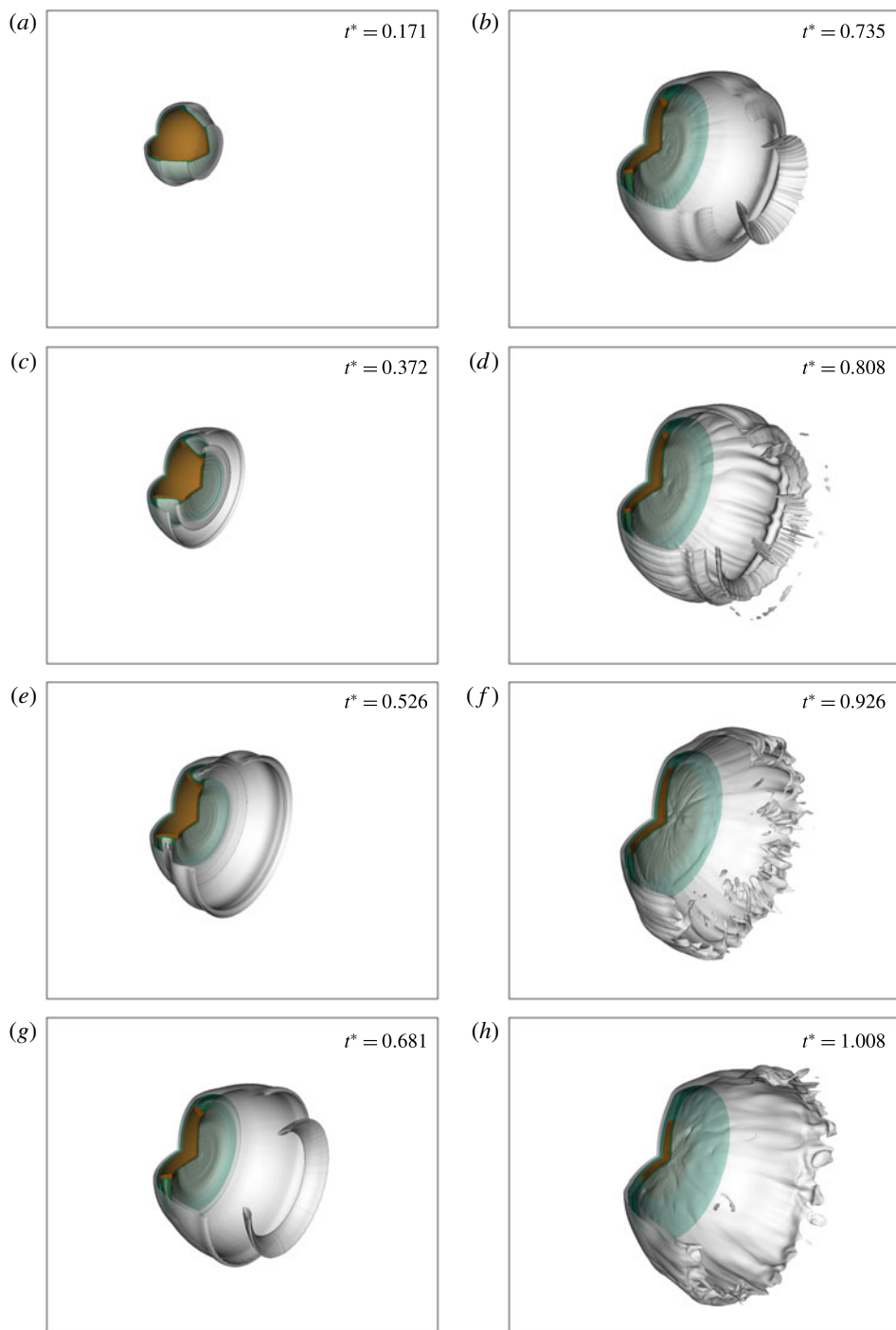
FIGURE 2. (Colour online) Isosurfaces of the liquid volume fraction, $\alpha_l = 0.99, 0.50, 0.01$ (orange, green, white). Flow is from top left to bottom right.
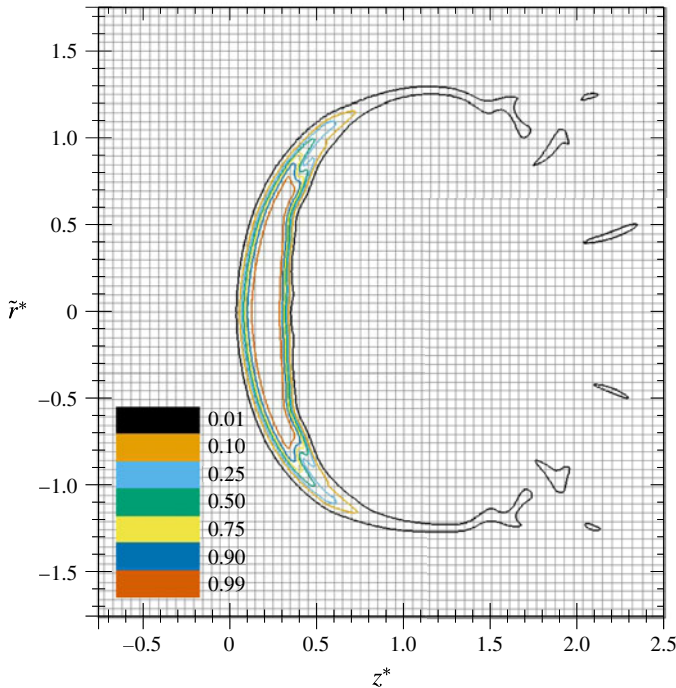
FIGURE 3. (Colour online) Sliced isopleths of α_l at $t^* = 0.799$ shown on the computational grid at $1:5$ of the actual resolution.

passage of the shock when the droplet is subject to constant acceleration. During this time period, the droplet is adjusting to the step change in ambient flow conditions, and is still well-approximated as a rigid sphere. This delay, which is not observed in 2D simulations (Meng & Colonius 2015) and is, perhaps, related to the flow-relieving effect of the third dimension, ceases when the droplet begins to pancake and its drag properties substantially change. Secondly, a dominant low-frequency oscillation is observed in the droplet's acceleration curve. In figure 5, we replot the acceleration curve using standard convective time units for flow past a rigid sphere, tu_s/D_0, to check if this low frequency corresponds with wake instability. The vertical gridlines are spaced $5D_0/u_s$ apart to coincide with the expected period of a wake instability (vortex shedding) which, for flow over a rigid sphere, occurs with Strouhal number $St = fD_0/u_s = 0.2$. The largest oscillations in the acceleration are roughly commensurate with this frequency, but owing to the relatively short data available, it is difficult to draw a firm conclusion.

Finally, figure 5(b) shows the droplet's unsteady drag coefficient, C_D. The frontal area used in the non-dimensionalization assumes a circular upstream projected area based on the droplet's deformed diameter, D_d. From figure 2, this assumption is seen to be a reasonable approximation for the times shown in figure 5. D_d is taken as the maximal spatial extents in the $\tilde{r}$-coordinate, which depends on the choice of α_l. Thus, in figure 5, we show bounds for the C_D spanning $0.25 \leqslant \alpha_l \leqslant 0.99$. For $t^* < 0.3$, the choice of α_l has little impact on the C_D. During the period of constant acceleration, and before the droplet has had sufficient time to significantly deform, we observe that the drag coefficient for a rigid sphere, $C_D = 0.5$, is approximately recovered. As the droplet begins pancaking, the drag coefficient transitions to be comparable to that for
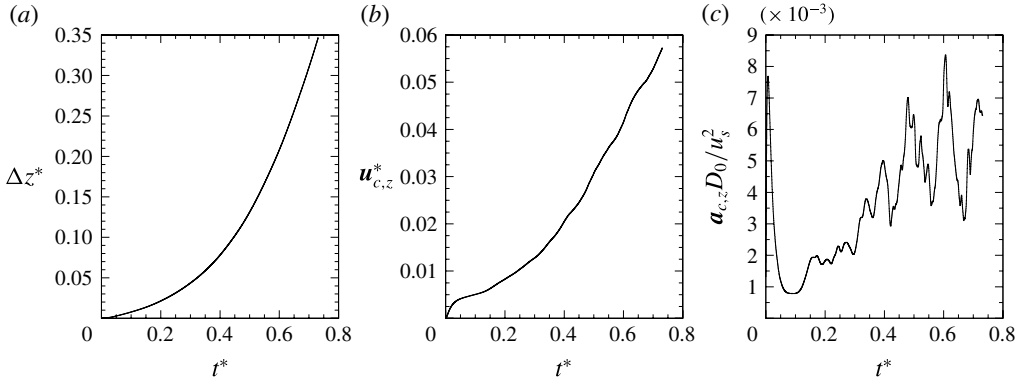
FIGURE 4. Droplet streamwise centre-of-mass (*a*) drift, (*b*) velocity, and (*c*) acceleration.
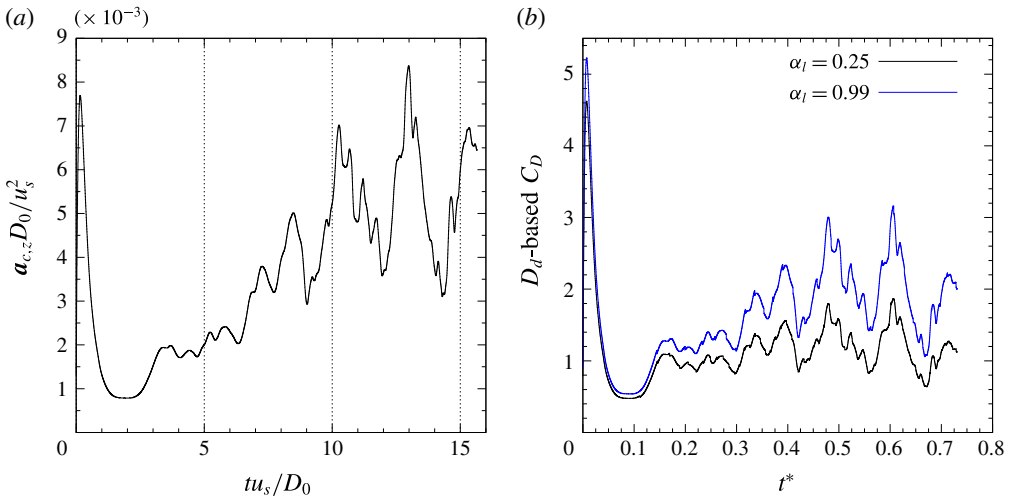

FIGURE 5. (Colour online) Droplet (*a*) acceleration in convective time units and (*b*) unsteady drag coefficient for a range of D_d (dependent upon choice of α_l).

a flat disk, which has $C_D \approx 1$. For $t^* > 0.3$, C_D depends more strongly on choice of α_l-value, representing the uncertainty in the deformed diameter. Unsteady effects begin to dominate and the drag coefficient subsequently exhibits fluctuations about an increasing average value. While it is impossible to state the true value of C_D, the oscillatory behaviour (present also in the acceleration time history) is believed to be physical, and the plot is thought to reasonably bound the physical values at late times.

4.2. *Comparison with experimental visualizations*

We now compare the simulated breakup with the experimental visualizations of Theofanous *et al.* (2012). They studied the breakup of water droplets (among other liquids) in a helium shock tube. Given the uncertainty in the exact interface location and the numerical diffusion of the material discontinuity, we compare the experimental images to both the $\alpha_l = 0.01$ isosurface and sliced isopleths for various α_l-values. Despite a mismatch in flow conditions and a dearth of timing data, our numerical
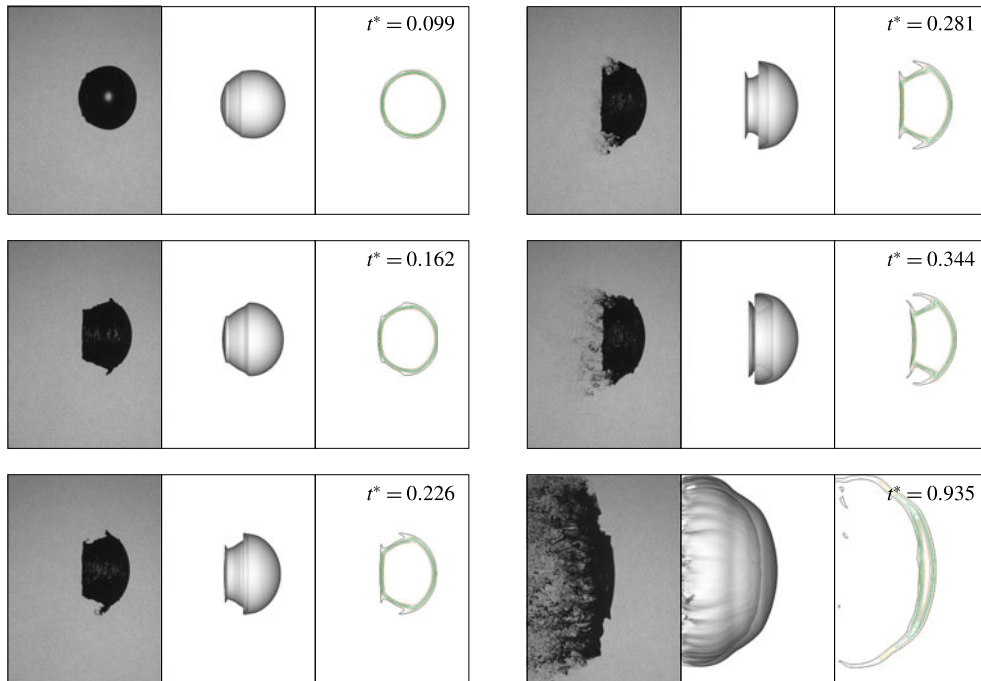
FIGURE 6. (Colour online) Comparisons with experimental visualizations of the aerobreakup of a water droplet from figure 33 of Theofanous *et al.* (2012). Flow is from right to left. Each frame consists of an experimental image reproduced from the video stored online (https://doi.org/10.1063/1.3680867.12) (left), the numerical $\alpha_l = 0.01$ isosurface (centre), and sliced isopleths of α_l (right) corresponding to the legend in figure 3. The timing information is for the numerical results; no experimental timing information is available.

results show good qualitative agreement with the experimental visualizations of the SIE phenomenology. The small value of the α_l-isosurface is believed to be a fair comparison for visualization purposes, as the experimental images are also obscured by the fine mist that is generated during breakup. Additionally, comparisons with the sliced isopleths confirm a qualitative agreement largely independent of the numerics.

The post-shock flow in the experiment has a Mach number of 0.32, which corresponds to experimental Reynolds and Weber numbers of $Re = 2.2 \times 10^4$ and $We = 780$. The large Reynolds and Weber numbers allow us to make qualitative comparisons with our numerical results. This comparison is shown in figure 6. First, we observe the same initial deformation of the droplet into a muffin-like shape. The upstream side of the droplet remains spherical, while the downstream side is flattened into a planar surface. What appears to be a thin liquid sheet coming from the spherical lip is visible beginning at $t^* = 0.162$. This sheet quickly disintegrates into a mist that obscures the coherent part of the droplet. The coherent droplet body is continually flattened in the streamwise direction, and liquid material is constantly stripped off near its equator. At late times in the SIE process, the liquid fragments form a cylindrical curtain around a cavity behind the coherent droplet. In figure 7, we compare experimental and numerical images of this liquid sheet. As discussed in §3.2, we do not capture the ultimate capillary-driven breakup of the liquid sheet.
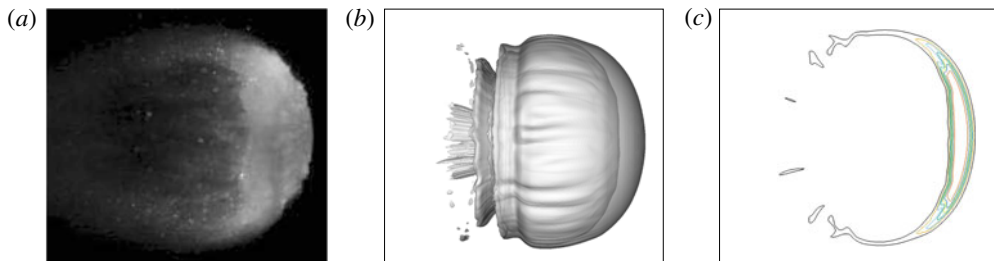
FIGURE 7. (Colour online) Comparison of experimental and numerical liquid 'curtains.' The experimental image taken from figure 17(*b*) of Theofanous *et al.* (2012) (*a*) is for Mach 0.59 flow at $t^* = 0.81$. The numerical isosurface of $\alpha_l = 0.01$ (*b*) and sliced isopleths of α_l (*c*) are for Mach 0.5775 flow at $t^* = 0.808$. Isopleth colours correspond to the legend in figure 3.

Though these experimental comparisons are not without uncertainty, we find that our numerical results are, by and large, not far off from the experimental visualizations of the SIE regime.

4.3. *Flow field in the gas*

From their experimental results, Liu & Reitz (1997) proposed a rough classification of the breakup process into two stages. They experimentally observed the first stage as a pressure-driven shape change of the droplet. This deformation stage, shared amongst multiple breakup regimes, is characterized by a flattening of the droplet in the streamwise direction. This pancaking is a consequence of the non-uniform pressure distribution around the droplet surface. High pressures at the forward and rear stagnation points, as well as low pressures at the equator due to the acceleration of the gas, both contribute to the flattening of the droplet. The second stage, as described by Liu & Reitz (1997), is characterized by droplet disintegration and is when the phenomenology diverges for the various breakup regimes. For the stripping regime, they observed the edges of the droplet being drawn out into a thin liquid sheet by drag forces, and the subsequent breakup of the sheet into fine ligaments.

Contrary to Liu & Reitz's description of the breakup process as two consecutive stages, our numerical results suggest that the phenomenology of stripping may be better described as the simultaneous flattening and stripping of liquid material. In fact, not only are the flattening and the disintegration processes occurring concurrently throughout the breakup process, they are also intricately connected by the dynamic behaviour of the surrounding gas flow.

In order to elucidate why the liquid behaves as it does, we look to the behaviour of the surrounding gas flow as visualized in figures 8 and 9 (images are ordered top to bottom, left to right). Figure 8 shows 2D slices taken through the centre of the droplet, x^*, $y^* = 0$, that are offset for unobstructed viewing of both planes. The vertical plots are coloured by velocity magnitude normalized by the post-shock gas velocity, $\|u\|^*$, while the horizontal plots are coloured by pressure, p^*. Isopleths of the numerical schlieren function, φ, reveal the intricate and dynamic flow structures that develop in the wake. Following Quirk & Karni (1996), the numerical schlieren function is computed as the exponential of the negative, normalized density gradient

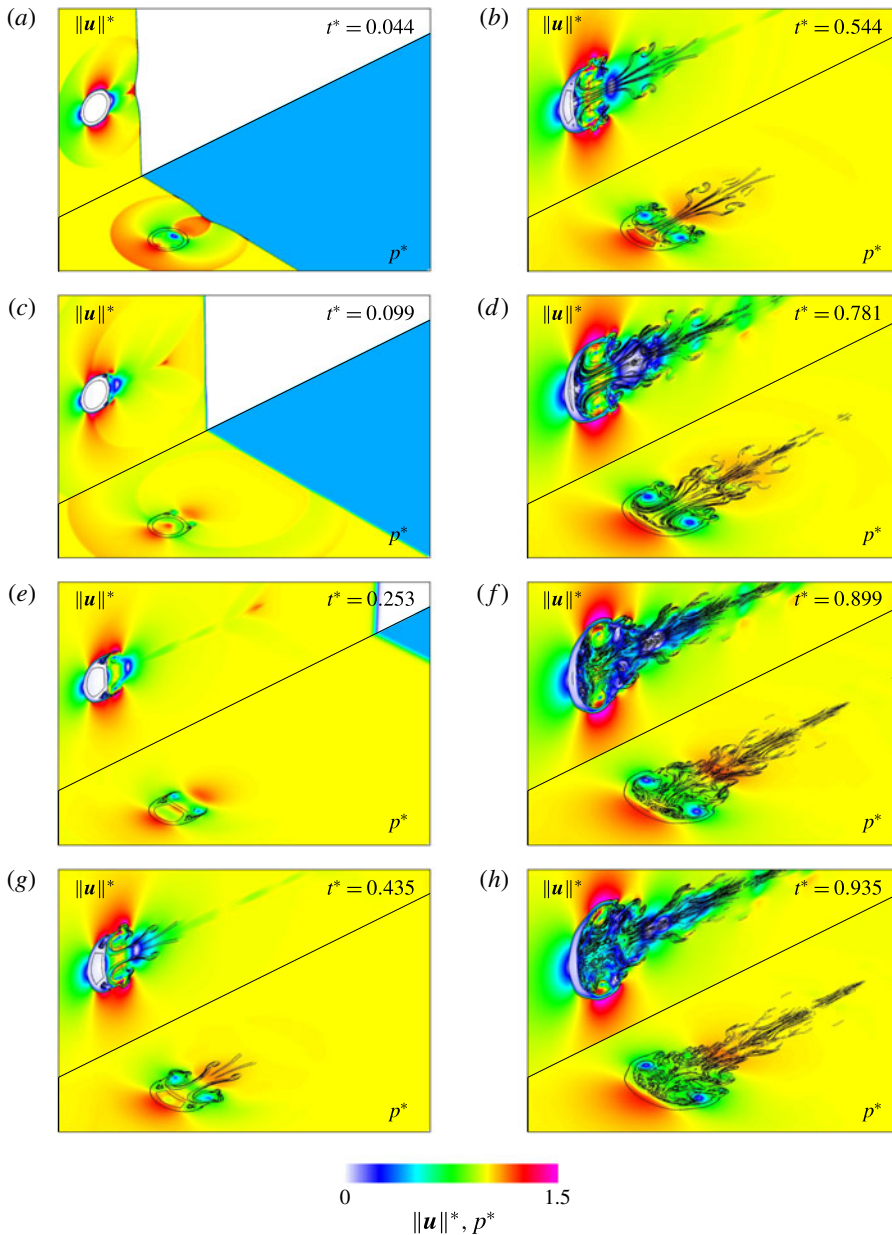$$\varphi = \exp\left(-\beta \frac{\|\nabla \rho\|}{\|\nabla \rho\|_{max}}\right), \tag{4.1}$$

FIGURE 8. (Colour online) Filled contour slices of velocity magnitude, $\|\boldsymbol{u}\|^*$, and pressure, p^*, and isopleths of the numerical schlieren function. Flow is from bottom left to top right. Offset 2D slices are taken at $x^* = 0$, $y^* = 0$.

where β is a scaling parameter that allows simultaneous visualization of waves in both fluids. Following Johnsen (2007), $\beta_{air} = 40$ and $\beta_{water} = 400$. The three-dimensionality of the aerobreakup process is well captured in figure 9, which plots various isosurfaces of azimuthal vorticity, ω_θ. Since the innermost regions of the flow are obstructed from view, slices are again taken through the centre of the drop and offset to both sides. The transverse slice, offset upstream of the droplet, is taken at $z^* = 1$.
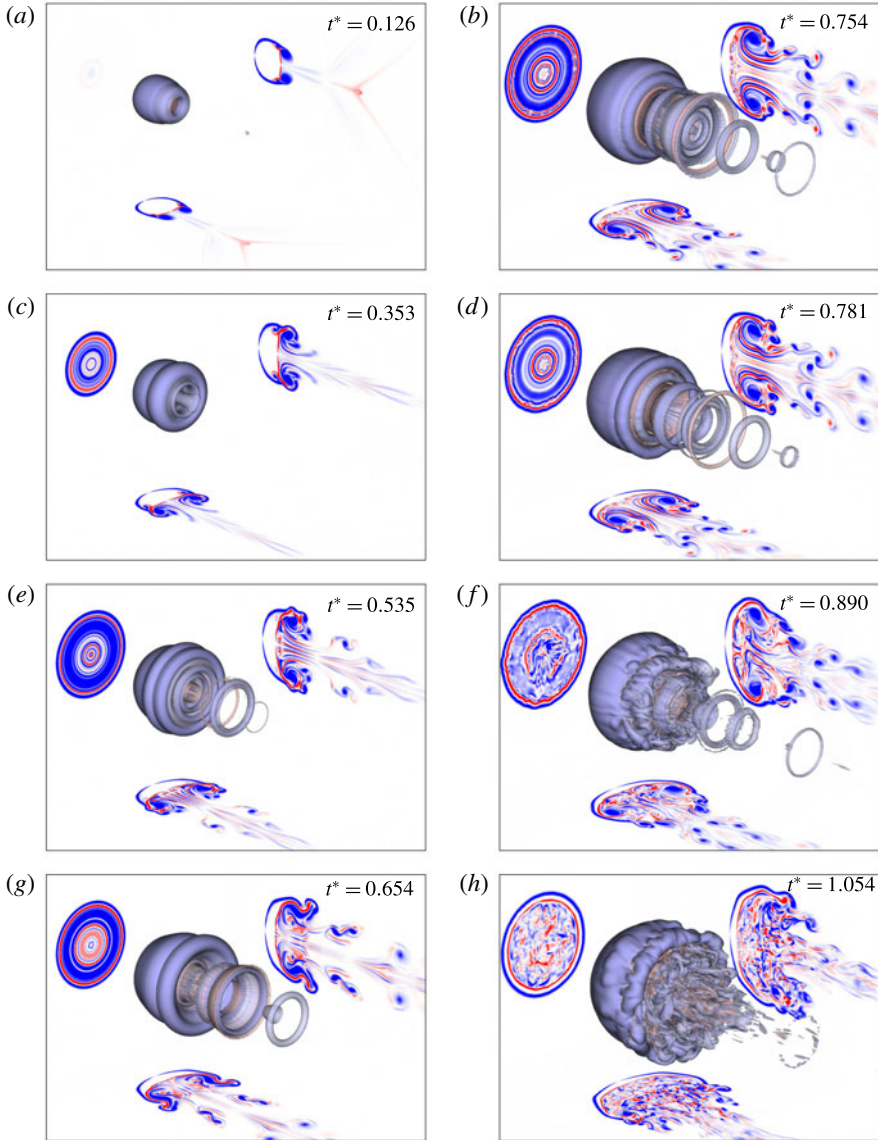
FIGURE 9. (Colour online) Isosurfaces of positive (red) and negative (blue) azimuthal vorticity, ω_θ. Flow is from top left to bottom right. Offset 2D slices are taken at $x^* = 0, y^* = 0, z^* = 1$.

The incident and reflected shock waves, as well as the secondary wave system generated by the convergence of Mach stems at the rear stagnation point, are visible in the first few snapshots of figure 8. The peak drag of the droplet is marked by the transition of the reflected shock from a regular reflection to a Mach reflection at some inclination angle preceding the droplet equator. This phenomenon has been studied in the literature for rigid cylinders and spheres (Takayama & Itoh 1986; Tanno *et al.* 2003), and is also observed in the case of 2D aerobreakup (Meng & Colonius 2015). Promptly after the passage of the incident shock, the flow is accelerated to

approximately $1.5u_s$ at the droplet's equator (pink colouring is visible at $t^* = 0.044$ in figure 8), which is the value expected from potential flow theory for flow past a rigid sphere. In the early stages of droplet deformation, $t^* \leqslant 0.435$, the transmitted wave that propagates into the liquid from the incident shock wave is observed to bounce back and forth within the droplet. From our numerical results and the aerobreakup literature, this transmitted wave inside the liquid droplet is not thought to play a significant role in the aerobreakup process.

As discussed earlier, the non-uniform pressure distribution around the droplet is the principal mechanism driving droplet deformation. This is clearly seen in the filled pressure contours of figure 8. Unlike the case of steady separated flow past a rigid sphere, the pressure at the rear stagnation point remains, during the initial flattening, larger than the pressure at the droplet's equator.

The equatorial recirculation region, visible in figure 9, is formed by the interaction of two opposite-sign azimuthal vorticity streams generated by baroclinicity. The formation of this equatorial recirculation region has previously been observed to also occur for 2D aerobreakup (Meng & Colonius 2015). Its location coincides with the sides of the muffin-shaped droplet behind the lip of the spherical upstream droplet surface. This equatorial recirculation region thus serves as a possible explanation for the muffin-like shape of the deformed droplet, and, for the duration of its existence, is at least partially responsible for the liquid sheets that are drawn out from both the spherical lip and the planar back of the droplet.

Other notable flow features visible in figure 8 include a wake recirculation region and two concentric shear layers at the droplet equator. Behind the droplet, the wake recirculation region is quickly established, as evidenced by the departure of the flow reversal region (i.e. the white patch in the wake directly behind the droplet where the streamwise velocity changes direction) from the rear stagnation point at $t^* = 0.099$ in figure 8 (at $t^* = 0.126$ in figure 9, the wake recirculation region already exists). The flow reversal patch also serves to demarcate the end of an upstream jet that is created in the wake. The wake recirculation region is bounded by shear layers that are subject to KH instability, and the unsteady vortex shedding drives the development of a complicated wake. KH roll-up and subsequent vortex shedding from the shear layers can be seen particularly clearly from the numerical schlieren isopleths at $t^* = 0.435, 0.544, 0.781$ in figure 8.

For clarity, it would be ideal if the aforementioned flow phenomena could be discussed separately as distinct flow features. However, in reality, they are so interconnected that such a disjoint discussion would be both incomplete and overly simplistic. In the remainder of this section, we attempt a comprehensive examination and discussion of these flow phenomena.

The formation of the wake recirculation region initiates a strongly coupled, self-sustaining set of flow phenomena that evolve with ever-increasing complexity. The wake recirculation region, created by the stream of negative azimuthal vorticity from the upstream side of the droplet, remains in the near-field wake region. It is perpetually sustained by the same vorticity stream, and entrains the surrounding fluid, which is pulled into an upstream jet that impinges on the rear stagnation point of the droplet.

This upstream jet, driven by the recirculation region, preserves high pressure at the rear stagnation point that contributes to both the pancaking of the coherent droplet, as well as the generation of positive vorticity along the back of the droplet. The positive vorticity is transported towards the equator by the recirculation region, and interacts with the negative vorticity stream to create, at early times, the equatorial

recirculation region. Some positive vorticity is also transported downstream, forming a parallel stream inside the negative vorticity stream coming from the upstream side of the droplet. The shear flow that is created when the upstream jet impinges on the back of the droplet may also contribute to the liquid sheet that arises from the downstream side.

As the equatorial liquid sheet is blown downstream by inertial forces from the surrounding gas flow, shear layers are formed on both sides of the sheet. The gas that is accelerating around the droplet creates shear on the exterior, while the wake recirculation region, that exists inside the cavity enveloped by the sheet, creates shear along the interior. Both the interior and exterior shear layers are visible in figure 8. As the liquid sheet flaps, generating longitudinal ripples, the shear layers, which are subject to KH instability, periodically shed vortices that are either entrained by the wake recirculation region, or are convected downstream. Entrained vortices (of both signs) by the wake recirculation region result in the upstream jet being characterized by concentric layers of alternating vorticity sign (visible from $t^* = 0.535$–0.781 in figure 9). Entrainment of shed vortices is also associated with a temporary increase in upstream jet velocity that results in a cyclic pumping of fluid onto the back side of the droplet. Downstream-convected vortices, that are not entrained, quickly lose their initial axisymmetry due to the instability of vortex rings, and subsequently develop into fully 3D flow features.

In time, as the liquid sheet is drawn downstream and the coherent droplet diameter expands laterally, the flow within the enveloped cavity at the back of the droplet, encompassing the wake recirculation region and the upstream jet, correspondingly grows in size and complexity. Loss of axisymmetry is observed to first occur in the core region of wake, i.e. small r. However, before it radially expands to encompass the entire wake region, another instability is observed to emerge along the still-axisymmetric positive vorticity sheet (located just inside the equatorial liquid sheet). From $t^* = 0.754$–0.781 in figure 9, we see what appear to be RT fingers or mushroom-like features propagating inwards towards the core that cause azimuthal rippling in the previously axisymmetric vorticity sheet. This instability, further discussed in §5, generates the transverse azimuthal modulations observable on the liquid sheet visible for $t^* \geqslant 0.808$ in figure 2. As the entire wake region devolves into chaotic, turbulent-like flow, the general coherence of the aforementioned phenomena is lost, as seen for $t^* \geqslant 1.054$ in figure 9. At these late times, the coherent droplet body presents an essentially blunt body to the oncoming free-stream flow such that the highest pressures are found on the upstream side of the flattened disk-like droplet.

5. Surface instabilities and transition

5.1. *Mechanism of instability*

The upstream side of a droplet undergoing aerobreakup is susceptible to RT instability waves that arise from the acceleration of the lighter gas into the denser liquid. In the classical catastrophic breakup regime, 'fingers of hot air' were thought to penetrate the droplet, leading to an explosive disintegration (Joseph *et al.* 1999). In contrast stands the recent of work of Theofanous & Li (2008) who observed that '[t]here are no RT waves piercing the drop...' Indeed, no RT waves are seen on the droplet in our numerical simulation. This is shown in figure 10, where the upstream side of the drop for various isopleths of α_l remains smooth for the entirety of the simulation. Our numerical results thus support Theofanous & Li's claim of SIE being the
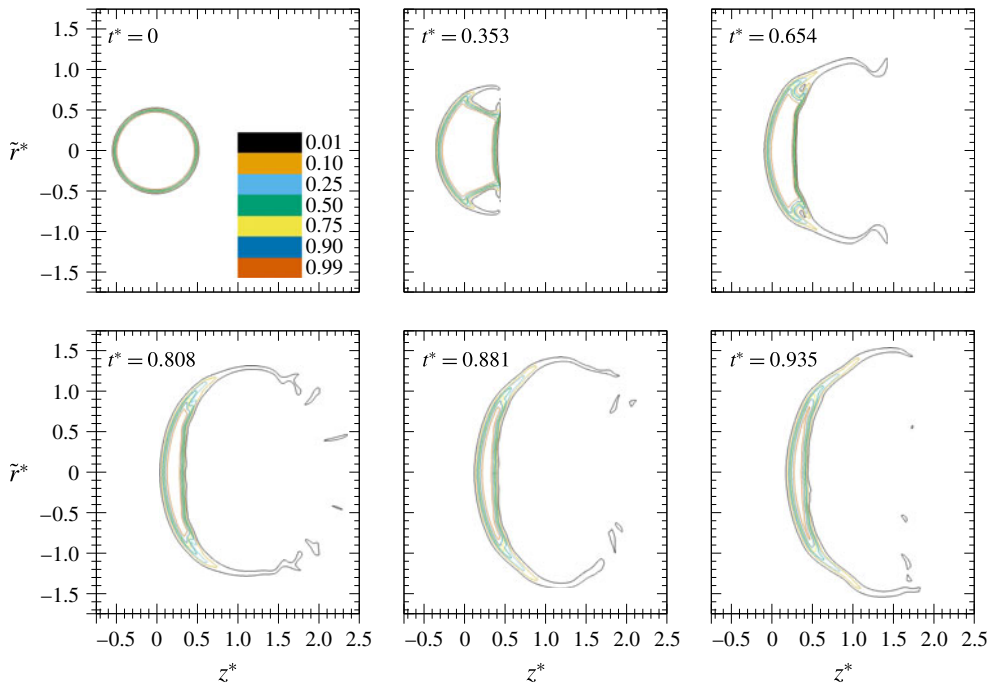
FIGURE 10. (Colour online) Sliced isopleths of α_l showing droplet profiles.

terminal breakup regime. The suppression of the RT instability waves was initially explained by Theofanous & Li (2008) to be a consequence of the stability of the stagnation flow (reminiscent of the lenticular shape of a gas bubble rising through liquid (Batchelor 1987)). More recently, an analysis of the viscous KH instability by Theofanous *et al.* (2012) found that '[w]ave numbers and growth factors of [KH] instability are consistently greater than those of [RT] instability by more than an order of magnitude... [T]he stretching further contributes to keeping this area mollified and free of any instability all the way to the end.'

In describing the instabilities that arise on the liquid sheet that lead to its disintegration, Liu & Reitz (1997) proposed the 'stretched streamwise ligament breakup' mechanism of Stapper & Samuelsen (1990). This breakup mechanism is characterized by the dominant formation and growth of streamwise vortical waves on the sheet, with thin membranes formed between them. 'Breakup occurs as the membranes are stretched thin by the rotation of the streamwise vortices and burst into small droplets. The streamwise vortical waves separate as streamwise ligaments, stretch and spin faster in the presence of the air shear, and eventually break up, contributing the larger drops to the final drop size distribution' (Stapper & Samuelsen 1990). From figure 11, which plots transverse slices of the liquid sheet at various streamwise locations, we see that our numerical results do not support this mechanism as the reason for sheet disintegration. Instead of a liquid sheet with variable thickness in the azimuthal coordinate, we observe relatively constant sheet thickness, and a rippling-type instability. Additionally, isosurfaces of the liquid sheet coloured by axial and radial vorticity, $\omega_{z,r}^* = \omega_{z,r} D_0/u_s$, (as shown in figure 12) suggest that streamwise (axial) vorticity (with its smaller magnitude) does not play a dominant role in the sheet breakup. It should be noted here that while figures 11 and 12 are plotted
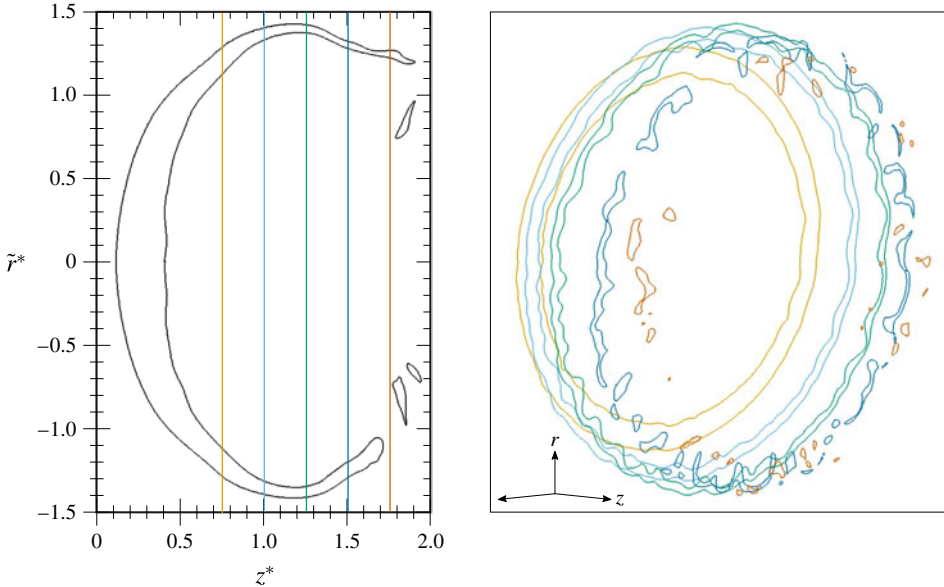
FIGURE 11. (Colour online) Transverse slices of the liquid sheet at $t^* = 0.881$, defined by $\alpha_l = 0.01$, at various streamwise locations.
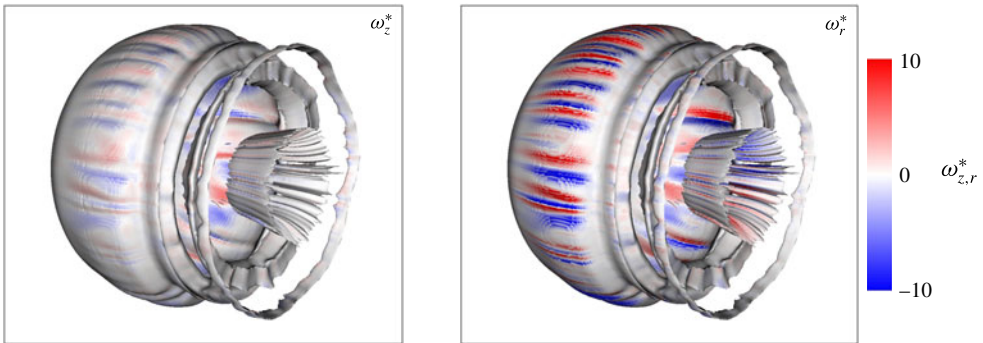

FIGURE 12. (Colour online) The liquid sheet coloured by axial and radial vorticity, $\omega_{z,r}^*$, at $t^* = 0.808$.

using the $\alpha_l = 0.01$ isosurface, the sheet thickness is still relatively constant in the azimuthal coordinate for other values of α_l (visible from figure 10), and the relative importance of ω_z^* is unchanged by the choice of α_l. In addition to the 'stretched streamwise ligament' mechanism of sheet breakup, Liu & Reitz (1997) also proposed another rippling mechanism based on mass conservation arguments. Though this remains a possibility, the observed phenomena are most likely the net result of several mechanisms. Given the modelling approximations and implications discussed in §3.2, no physical length scales can be associated with the instabilities that are observed in the numerical results. Instead, we are limited to qualitatively describing the observed phenomena.

Jalaal & Mehravaran (2014) proposed the RT instability as the source of the transverse azimuthal modulations. Arguing that the accelerated liquid sheet is subject
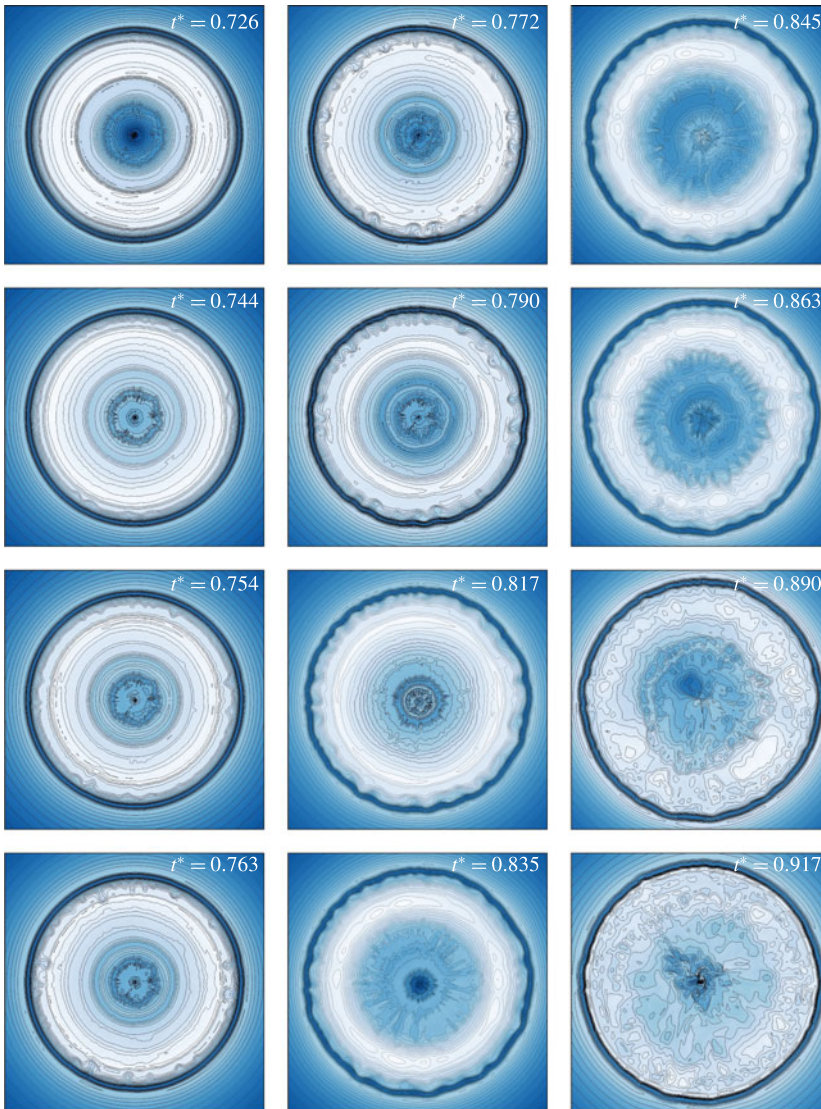
FIGURE 13. (Colour online) Filled contours and isopleths of gas partial density, $\alpha_g \rho_g$, at $z^* = 1$. Darker colours correspond to larger densities (colouring and isopleth values vary between frames).

to the same instability as that which forms streamwise ligaments in the case of a round liquid jet in coaxial flow, they attempted a quantitative comparison with theory, but found only marginal agreement. The general concept, though, of RT instability on the liquid sheet may, indeed, have merit, and supporting (qualitative) evidence can be found in our numerical results. As noted at the end of §4.3, RT fingers or mushroom-like features are seen emerging along the positive vorticity sheet that lies just inside the equatorial liquid sheet. To relate these features to the RT instability, we plot filled contours and isopleths of the gas partial density for late times in figure 13. At $t^* = 0.726$, the axisymmetry of the outer regions of the wake is still preserved, as
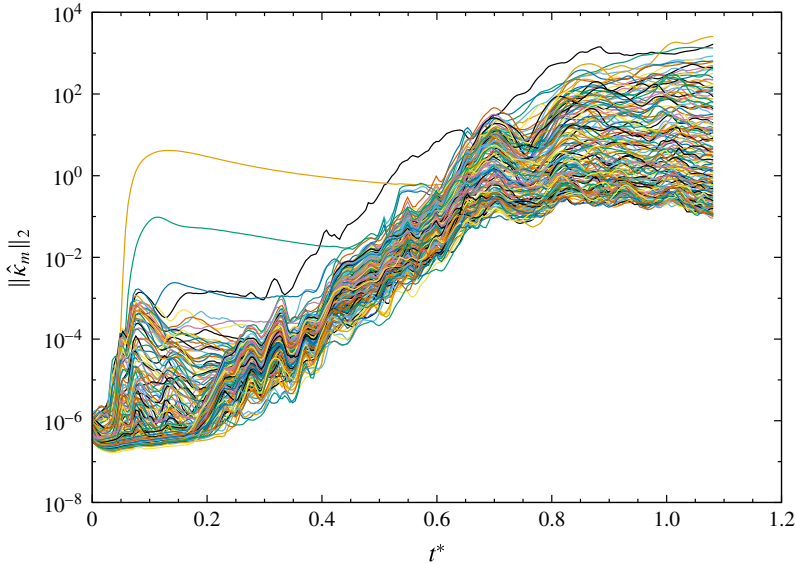
FIGURE 14. (Colour online) L_2-norm of the (kinetic) energy (see (5.1)) for each of the $N_\theta/2$ modes resulting from the azimuthal Fourier decomposition of the velocity field.

evidenced by the circular isopleths. From $t^* = 0.744$–0.790, however, the axisymmetry is broken by multiple fingers of denser gas propagating towards the axis into the lighter gas (darker colours correspond to larger densities). These fingers correspond exactly with the indentations generated on the liquid sheet. Not long after this loss of outer axisymmetry, the entire wake region degenerates into a chaotic, turbulent-like flow with complete loss of flow feature coherence.

5.2. *Azimuthal Fourier decomposition*

Motivated by the observed azimuthal modulations, we perform a Fourier decomposition of the velocity flow field to determine if a particular mode(s) or wavenumber(s) is associated with the loss of axisymmetry. To do this, we take a Fourier transform in the θ-coordinate to obtain the Fourier coefficients of each of the azimuthal modes, $\hat{\boldsymbol{u}}_m(z, r, t)$. We then calculate an energy metric for each mode defined as

$$\hat{\kappa}_m = |\hat{u}_{z,m}|^2 + |\hat{u}_{r,m}|^2 + |\hat{u}_{\theta,m}|^2, \tag{5.1}$$

where the hat denotes the Fourier transform in the θ-coordinate. Taking an L_2-norm of $\hat{\kappa}_m$ over the entire computational domain, we plot the time histories of $\|\hat{\kappa}_m\|_2$ for each of the $N_\theta/2$ modes (excluding the mean) in figure 14. Notably, the frequency response of the system shows broadband instability growth for all modes. An initial jolt applied to the system by the passage of the shock wave is mostly stabilized after approximately $t^* = 0.1$. This is followed by the exponential growth of nearly all wavenumbers. If we view the interaction of the incident shock with the droplet as an impulsive force applied to the system, the broadband instability response is not surprising. Four of the modes appear to exhibit a different type of behaviour; however, these unusual curves are actually artefacts of the random velocity perturbations seeded in the initial condition. Unfortunately, due to the unsteady, non-stationary, and
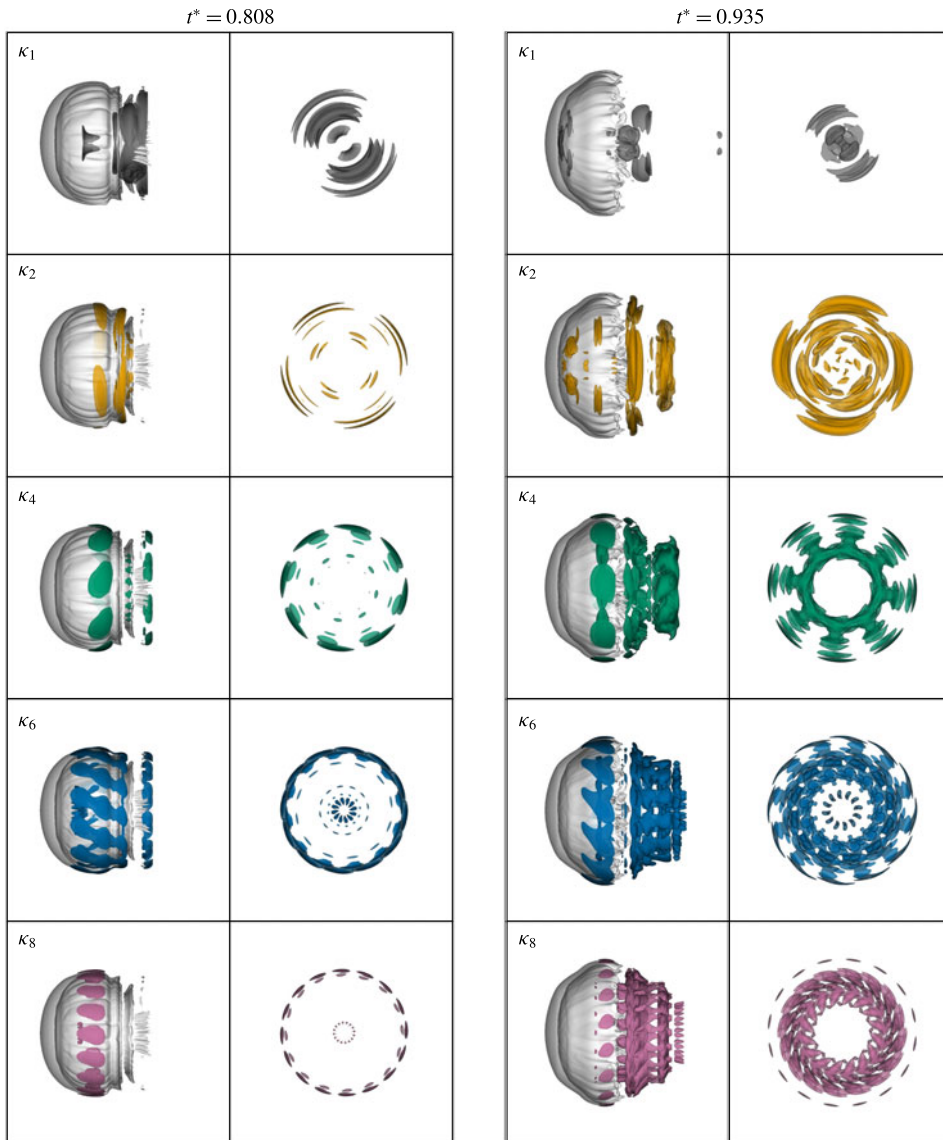
FIGURE 15. (Colour online) Isosurfaces of κ_m, $m = 1, 2, 4, 6, 8$ at $t^* = 0.808, 0.935$. Also shown is a cut isosurface of the liquid sheet visualized using $\alpha_l = 0.01$. Front and side views are shown, and isosurface values change between frames.

nonlinear nature of the aerobreakup problem, this type of instability analysis is unable to pick out a dominant mode or wavenumber associated with the loss of axisymmetry. Despite the broadband response, visualization of the first few modes transformed back into θ-space, $\kappa_m = u_{z,m}^2 + u_{r,m}^2 + u_{\theta,m}^2$, reveals some interesting observations about the development of the wake, and offers some general intuition about the physical spatial structure of κ_m. Figure 15 shows the isosurfaces of a few modes at late times in the simulation, $t^* = 0.808, 0.935$, when all frequencies have saturated (see figure 14). From figure 15, we see that the structures are initially clustered around the location

of the liquid sheet, and subsequently grow in size and complexity. Even at late times, the structures remain bounded by the wake region. Streaky streamwise-oriented flow structures near the wake core, visible for $\kappa_{6,8}$ at $t^* = 0.808$, appear to be related to the loss of axisymmetry in the upstream jet region, while the outer structures are linked to the liquid sheet and shear layers. As this broadband instability is not directly associated with any classical hydrodynamic instability, we are unable to relate these κ_m-structures to other recognizable flow features.

6. Conclusions

In this paper, we have presented the first detailed description of the underlying flow physics associated with droplet deformation during stripping aerobreakup. The droplet morphology is first described and compared to experimental visualizations of the SIE process. Good qualitative agreement is found in terms of the droplet's initial deformation into a muffin-like shape, followed by the disintegration of a liquid sheet that envelops a cavity in the near-field wake region.

The droplet's centre-of-mass properties reveal significant unsteadiness in the droplet's acceleration, which oscillates with a frequency that roughly matches the Strouhal number associated with wake instability. Limitations on the available data, however, make it difficult to draw a firm conclusion. The droplet's unsteady drag coefficient, when normalized using the deformed droplet diameter, briefly recovers that for a rigid sphere during the very early stages of aerobreakup. Subsequently, the droplet's deformation alters its drag properties and unsteady effects become dominant as the drag coefficient oscillates about an increasing average value.

Numerical visualizations of the surrounding flow behaviour provide insights into the experimentally observed drop morphology. At early times, the existence of the equatorial recirculation region, comprised of two counter-rotating vortices, explains both the muffin-like shape, and the pulling of liquid sheets from both the droplet's equator and its flattened back. The enveloped cavity attached to the downstream side of the deforming droplet is associated with a recirculation region that entrains fluid and jets it upstream to impinge on the rear stagnation point. The shear layers that form on both sides of the liquid sheet are subject to KH instability, and shed vortices that are either convected downstream or entrained by the wake recirculation region. RT instability waves on the upstream side of the droplet are noticeably absent, providing support for SIE as the terminal breakup regime.

Analyses of the instabilities arising on the liquid sheet reveal discrepancies with the proposed 'stretched streamwise ligament breakup' mechanism, while some qualitative evidence for the rise of RT instability along the accelerated sheet can be found. An attempt is made to find particular modes associated with the loss of axisymmetry by performing an azimuthal Fourier decomposition of the flow field. Unfortunately, due to the unsteady and nonlinear nature of the aerobreakup problem, this analysis is limited in its efficacy, and instead shows broadband instability growth of all modes, as would be expected from impulsive forcing of the system.

Appendix A. State variables, fluxes, and source terms

The vector of conservative variables, $\boldsymbol{q}$:

$$\boldsymbol{q} = \begin{pmatrix} \alpha_1\rho_1 \\ \alpha_2\rho_2 \\ \rho u_z \\ \rho u_r \\ \rho u_\theta \\ E \\ \alpha_1 \end{pmatrix}. \tag{A 1}$$

The flux vectors, $\boldsymbol{f}(\boldsymbol{q}), \boldsymbol{g}(\boldsymbol{q})$ and $\boldsymbol{h}(\boldsymbol{q})$:

$$\boldsymbol{f}(\boldsymbol{q}) = \begin{pmatrix} \alpha_1\rho_1 u_z \\ \alpha_2\rho_2 u_z \\ \rho u_z^2 + p \\ \rho u_r u_z \\ \rho u_\theta u_z \\ (E+p)u_z \\ \alpha_1 u_z \end{pmatrix}, \quad \boldsymbol{g}(\boldsymbol{q}) = \begin{pmatrix} \alpha_1\rho_1 u_r \\ \alpha_2\rho_2 u_r \\ \rho u_z u_r \\ \rho u_r^2 + p \\ \rho u_\theta u_r \\ (E+p)u_r \\ \alpha_1 u_r \end{pmatrix}, \quad \boldsymbol{h}(\boldsymbol{q}) = \frac{1}{r}\begin{pmatrix} \alpha_1\rho_1 u_\theta \\ \alpha_2\rho_2 u_\theta \\ \rho u_z u_\theta \\ \rho u_r u_\theta \\ \rho u_\theta^2 + p \\ (E+p)u_\theta \\ \alpha_1 u_\theta \end{pmatrix}. \tag{A 2a--c}$$

The source term vector, $\boldsymbol{s}(\boldsymbol{q})$:

$$\boldsymbol{s}(\boldsymbol{q}) = -\frac{1}{r}\begin{pmatrix} \alpha_1\rho_1 u_r \\ \alpha_2\rho_2 u_r \\ \rho u_z u_r \\ \rho(u_r^2 - u_\theta^2) \\ 2\rho u_r u_\theta \\ (E+p)u_r \\ \alpha_1(u_r - r\nabla\cdot\boldsymbol{u}) \end{pmatrix}. \tag{A 3}$$

The velocity divergence term in $\boldsymbol{s}(\boldsymbol{q})$ is necessary to adapt the non-conservative form of (2.1*e*) to the Riemann solver (Johnsen & Colonius 2006).

REFERENCES

AALBURG, C., LEER, B. V. & FAETH, G. M. 2003 Deformation and drag properties of round drops subjected to shock-wave disturbances. *AIAA J.* **41** (12), 2371–2378.

ALLAIRE, G., CLERC, S. & KOKH, S. 2002 A five-equation model for the simulation of interfaces between compressible fluids. *J. Comput. Phys.* **181**, 577–616.

BATCHELOR, G. K. 1987 The stability of a large gas bubble rising through liquid. *J. Fluid Mech.* **184**, 399–422.

CASTRILLON ESCOBAR, S., RIMBERT, N., MEIGNEN, R., HADJ-ACHOUR, M. & GRADECK, M. 2015 Direct numerical simulations of hydrodynamic fragmentation of liquid metal droplets by a water flow. In *13th Triennial International Conference on Liquid Atomization and Spray Systems*. ILASS.

CHANG, C. H., DENG, X. & THEOFANOUS, T. G. 2013 Direct numerical simulation of interfacial instabilities: a consistent, conservative, all-speed, sharp-interface method. *J. Comput. Phys.* **242**, 946–990.

CHEN, H. 2008 Two-dimensional simulation of stripping breakup of a water droplet. *AIAA J.* **46** (5), 1135–1143.

CORALIC, V. 2015 Simulation of shock-induced bubble collapse with application to vascular injury in shockwave lithotripsy. PhD thesis, California Institute of Technology, Pasadena, CA.

CORALIC, V. & COLONIUS, T. 2013 Shock-induced collapse of a bubble inside a deformable vessel. *Eur. J. Mech.* (*B/Fluids*) **40**, 64–74.

CORALIC, V. & COLONIUS, T. 2014 Finite-volume WENO scheme for viscous compressible multicomponent flows. *J. Comput. Phys.* **274**, 95–121.

ENGEL, O. G. 1958 Fragmentation of waterdrops in the zone behind an air shock. *J. Res. Natl Bur. Stand.* **60** (3), 245–280.

GOJANI, A. B., OHTANI, K., TAKAYAMA, K. & HOSSEINI, S. H. R. 2016 Shock Hugoniot and equations of states of water, castor oil, and aqueous solutions of sodium chloride, sucrose, and gelatin. *Shock Waves* **26** (1), 63–68.

GUILDENBECHER, D. R., LÓPEZ-RIVERA, C. & SOJKA, P. E. 2009 Secondary atomization. *Exp. Fluids* **46**, 371–402.

HAN, J. & TRYGGVASON, G. 2001 Secondary breakup of axisymmetric liquid drops. Part II. Impulsive acceleration. *Phys. Fluids* **13** (6), 1554–1565.

HANSON, A. R., DOMICH, E. G. & ADAMS, H. S. 1963 Shock tube investigation of the breakup of drops by air blasts. *Phys. Fluids* **6** (8), 1070–1080.

HARLOW, F. H. & AMSDEN, A. A. 1971 Fluid dynamics. *Tech. Rep.* LA-4700. LASL.

HINZE, J. O. 1949 Critical speeds and sizes of liquid globules. *Appl. Sci. Res.* **A1**, 273–288.

HSIANG, L. P. & FAETH, G. M. 1992 Near-limit drop deformation and secondary breakup. *Intl J. Multiphase Flow* **18** (5), 635–652.

HSIANG, L. P. & FAETH, G. M. 1995 Drop deformation and breakup due to shock wave and steady disturbances. *Intl J. Multiphase Flow* **21** (4), 545–560.

IGRA, D. & TAKAYAMA, K. 2001a Experimental and numerical study of the initial stages in the interaction process between a planar shock wave and a water column. In *23rd International Symposium on Shock Waves*. The University of Texas at Arlington.

IGRA, D. & TAKAYAMA, K. 2001b Numerical simulation of shock wave interaction with a water column. *Shock Waves* **11**, 219–228.

IGRA, D. & TAKAYAMA, K. 2001c A study of shock wave loading on a cylindrical water column. *Tech. Rep.* vol. 13, pp. 19–36. Institute of Fluid Science, Tohoku University.

JAIN, M., PRAKASH, R. S., TOMAR, G. & RAVIKRISHNA, R. V. 2015 Secondary breakup of a drop at moderate Weber numbers. *Proc. R. Soc. Lond.* A **471**, 20140930.

JALAAL, M. & MEHRAVARAN, K. 2014 Transient growth of droplet instabilities in a stream. *Phys. Fluids* **26**, 012101.

JOHNSEN, E. 2007 Numerical simulations of non-spherical bubble collapse with applications to shockwave lithotripsy. PhD thesis, California Institute of Technology, Pasadena, CA.

JOHNSEN, E. & COLONIUS, T. 2006 Implementation of WENO schemes in compressible multicomponent flow problems. *J. Comput. Phys.* **219**, 715–732.

JOHNSEN, E. & COLONIUS, T. 2009 Numerical simulations of non-spherical bubble collapse. *J. Fluid Mech.* **629**, 231–262.

JOSEPH, D. D., BELANGER, J. & BEAVERS, G. S. 1999 Breakup of a liquid drop suddenly exposed to a high-speed airstream. *Intl J. Multiphase Flow* **25**, 1263–1303.

KAPILA, A. K., MENIKOFF, R., BDZIL, J. B., SON, S. F. & STEWART, D. S. 2001 Two-phase modeling of deflagration-to-detonation transition in granular materials: reduced equations. *Phys. Fluids* **13** (10), 3002–3024.

KHOSLA, S., SMITH, C. E. & THROCKMORTON, R. P. 2006 Detailed understanding of drop atomization by gas crossflow using the volume of fluid method. In *19th Annual Conference on Liquid Atomization and Spray Systems*. ILASS.

LANE, W. R. 1951 Shatter of drops in streams of air. *Ind. Engng Chem.* **43** (6), 1312–1317.

LIU, Z. & REITZ, R. D. 1997 An analysis of the distortion and breakup mechanisms of high speed liquid drops. *Intl J. Multiphase Flow* **23** (4), 631–650.

MENG, J. C. 2016 Numerical simulations of droplet aerobreakup. PhD thesis, California Institute of Technology, Pasadena, CA.

MENG, J. C. & COLONIUS, T. 2015 Numerical simulations of the early stages of high-speed droplet breakup. *Shock Waves* **25** (4), 399–414.

MOHSENI, K. & COLONIUS, T. 2000 Numerical treatment of polar coordinate singularities. *J. Comput. Phys. Note* **157**, 787–795.

MURRONE, A. & GUILLARD, H. 2005 A five equation reduced model for compressible two phase flow problems. *J. Comput. Phys.* **202**, 664–698.

PELANTI, M. & SHYUE, K. M. 2014 A mixture-energy-consistent six-equation two-phase numerical model for fluids with interfaces, cavitation and evaporation waves. *J. Comput. Phys.* **259**, 331–357.

PERIGAUD, G. & SAUREL, R. 2005 A compressible flow model with capillary effects. *J. Comput. Phys.* **209**, 139–178.

PILCH, M. & ERDMAN, C. A. 1987 Use of breakup time data and velocity history data to predict the maximum size of stable fragments for acceleration-induced breakup of a liquid drop. *Intl J. Multiphase Flow* **13** (6), 741–757.

QUAN, S. & SCHMIDT, D. P. 2006 Direct numerical study of a liquid droplet impulsively accelerated by gaseous flow. *Phys. Fluids* **18**, 102103.

QUIRK, J. J. & KARNI, S. 1996 On the dynamics of a shock-bubble interaction. *J. Fluid Mech.* **318**, 129–163.

RANGER, A. A. & NICHOLLS, J. A. 1968 Aerodynamic shattering of liquid drops. In *AIAA 6th Aerospace Sciences Meeting*. AIAA.

SAUREL, R., PETITPAS, F. & BERRY, R. A. 2009 Simple and efficient relaxation methods for interfaces separating compressible fluids, cavitating flows and shocks in multiphase mixtures. *J. Comput. Phys.* **228**, 1678–1712.

SIMPKINS, P. G. & BALES, E. L. 1972 Water-drop response to sudden accelerations. *J. Fluid Mech.* **55**, 629–639.

STAPPER, B. E. & SAMUELSEN, G. S. 1990 An experimental study of the breakup of a two-dimensional liquid sheet in the presence of co-flow air shear. In *AIAA 28th Aerospace Sciences Meeting*. AIAA.

TAKAYAMA, K. & ITOH, K. 1986 Unsteady drag over cylinders and aerofoils in transonic shock tube flows. *Tech. Rep.* vol. 51. Institute of High Speed Mechanics, Tohoku University, Sendai, Japan.

TANNO, H., ITOH, K., SAITO, T., ABE, A. & TAKAYAMA, K. 2003 Interaction of a shock with a sphere suspended in a vertical shock tube. *Shock Waves* **13**, 191–200.

THEOFANOUS, T. G. 2011 Aerobreakup of Newtonian and viscoelastic liquids. *Annu. Rev. Fluid Mech.* **43**, 661–690.

THEOFANOUS, T. G. & LI, G. J. 2008 On the physics of aerobreakup. *Phys. Fluids* **20**, 052103.

THEOFANOUS, T. G., LI, G. J. & DINH, T. N. 2004 Aerobreakup in rarefied supersonic gas flows. *Trans. ASME J. Fluid Engng* **126**, 516–527.

THEOFANOUS, T. G., MITKIN, V. V., NG, C. L., CHANG, C. H., DENG, X. & SUSHCHIKH, S. 2012 The physics of aerobreakup. Part II. Viscous liquids. *Phys. Fluids* **24**, 022104.

WADHWA, A. R., MAGI, V. & ABRAHAM, J. 2007 Transient deformation and drag of decelerating drops in axisymmetric flows. *Phys. Fluids* **19**, 113301.

XIAO, F., DIANAT, M. & MCGUIRK, J. J. 2014 Large eddy simulation of single droplet and liquid jet primary breakup using a coupled level set/volume of fluid method. *Atomiz. Sprays* **24** (4), 281–302.

ZALESKI, S., LI, J. & SUCCI, S. 1995 Two-dimensional Navier–Stokes simulation of deformation and breakup of liquid patches. *Phys. Rev. Lett.* **75** (2), 244–247.